



science.sciencemag.org/cgi/content/full/science.abd9909/DC1

Supplementary Material for

De novo design of picomolar SARS-CoV-2 miniprotein inhibitors

Longxing Cao, Inna Goreschnik, Brian Coventry, James Brett Case, Lauren Miller, Lisa Kozodoy, Rita E. Chen, Lauren Carter, Alexandra C. Walls, Young-Jun Park, Eva-Maria Strauch, Lance Stewart, Michael S. Diamond, David Veessler, David Baker*

*Corresponding author. E-mail: dabaker@uw.edu

Published 9 September 2020 as *Science* First Release
DOI: [10.1126/science.abd9909](https://doi.org/10.1126/science.abd9909)

This PDF file includes:

Materials and Methods

Figs. S1 to S14

Tables S1 to S3

References

De novo design of picomolar SARS-CoV-2 miniprotein inhibitors

Longxing Cao^{1,2}, Inna Goreshnik^{1,2}, Brian Coventry^{1,2,3}, James Brett Case⁴, Lauren Miller^{1,2}, Lisa Kozodoy^{1,2}, Rita E. Chen^{4,5}, Lauren Carter^{1,2}, Alexandra C. Walls¹, Young-Jun Park¹, Eva-Maria Strauch⁶, Lance Stewart^{1,2}, Michael S. Diamond^{4,7}, David Veessler¹, David Baker^{1,2,8*}

1. Department of Biochemistry, University of Washington, Seattle, WA 98195

2. Institute for Protein Design, University of Washington, Seattle, WA 98195

3. Molecular Engineering Graduate Program, University of Washington, Seattle, WA 98195

4. Department of Medicine, Washington University School of Medicine, St. Louis, MO 63110, USA

5. Department of Pathology and Immunology, Washington University School of Medicine, St. Louis, MO 63110, USA

6. Dept. of Pharmaceutical and Biomedical Sciences, University of Georgia, Athens, GA 30602, USA

7. The Andrew M. and Jane M. Bursky Center for Human Immunology & Immunotherapy Programs, Washington University School of Medicine, St. Louis, MO 63110, USA

8. Howard Hughes Medical Institute, University of Washington, Seattle, WA 98195

*Corresponding author. E-mail: dabaker@uw.edu

Material and Methods

Designing miniprotein binders based on the ACE2 helix

The crystal structure (PDB: 6M0J) of the RBD bound to ACE2 (4) was refined with the Rosetta FastRelax protocol with coordinate constraints, and the main binding helix of ACE2 (residue 23 - 46) was extracted and used as the starting point for miniprotein generation. Miniprotein binder generation began by defining a variety of 3-helical bundles using the RosettaRemodel blueprint (18) format with the requirement that the ACE2 helix was incorporated into one of the helices. 1,974 blueprints that differed in the lengths of the helices and the loop types were generated. The blueprints were used to generate backbones using the Rosetta Monte Carlo-based fragment assembly protocol (19), while keeping the ACE2 helix fixed. Specially, the RBD structure was loaded into a hashing grid for fast clash checking to guarantee the newly generated backbones are not clashing with the RBD. The generated miniprotein was subjected to a 3 stage sequence design protocol. Firstly, only interface residues on the miniproteins were designed using the PackRotamersMover to quickly select designs that could make extra contacts with RBD besides the ACE2 helix. The whole miniprotein except the key interacting residues on the ACE2 helix were then designed using the FastDesign protocol, activating between side-chain rotamer optimization and gradient-descent-based energy minimization. Lastly, the interface residues were further optimized with another round of FastDesign to improve shape and chemical complementarity. The monomeric metrics and the interface metrics were calculated using Rosetta. Top 5,000 designs were selected based on the protein folding metrics (score_pre_res, buried non-polar area, local structure and sequence agreement) and interface metrics (ddg, shape complementarity, interface buried solvent accessible area). Both the quality of the designed monomeric structure and the accuracy of designed interface interactions are important for successfully making miniprotein binders, which is hard to achieve through one Monte Carlo fragment assembly trajectory. Thus, we performed a second round design based on the above generated design models. In detail, 273 helix hairpins that make good contacts with the RBD are

selected based on the above mentioned interface metrics. Starting from these helix hairpins, the third helix was built using the same fragment assembly protocol. Sequence design was performed on the generated backbone, except the first stage sequence design was omitted. The outputs were filtered by protein folding metrics and interface binding metrics, and 18,000 designs were selected. AHB2 were generated using the Round2 protocol using the interface helical hairpin of AHB1.

De novo binder design

The crystal structure (PDB: 6M0J) of the RBD bound to ACE2 (4) was refined with the Rosetta FastRelax protocol with coordinate constraints, and the RBD subunit was extracted for subsequent steps. Initial docking conformations were generated by RifDock (12). Briefly, billions of individual disembodied amino acids were docked against the ACE2 binding region on RBD using RifDock. The ones that passed a specific energy cutoff value (-1.5 Rosetta energy unit) were stored and the corresponding inverse rotamers were generated. The de novo scaffold library (11) of 19,000 mini-proteins (in length 56 - 65 residues) were docked into the field of the inverse rotamers to produce initial docked conformations. These docked conformations were further optimized using the FastDesign protocol to generate shape and chemically complementary interfaces. Computational metrics of the final design models were calculated using Rosetta, which includes ddg, shape complementary and interface buried solvent accessible surface area. Top 100,000 designs based on the above metrics were selected and an Agilent DNA library were ordered for DNA synthesis.

DNA library preparation

All protein sequences were padded to a uniform length (88 aa for approach 1 and 65 for approach 2) by adding a (GGGS)_n linker at the C terminal of the designs, to avoid the biased amplification of short DNA fragments during PCR reactions. The protein sequences were reversed translated and optimized using DNAworks2.0 (20) with the *S. cerevisiae* codon frequency table. Homologous to the pETCON plasmid Oligo libraries encoding the ACE2 helix scaffolded designs were ordered from Twist Bioscience. Oligo pool encoding the *de novo* designs and the point mutant library were ordered from Agilent Technologies. The error-prone library of the initial hit of the ACE2 helix scaffolded design was constructed by error-prone PCR with a GeneMorph II Random Mutagenesis Kit (Agilent Technologies) with manufacturer's instructions. 3 to 4 mutations were found on each sequence as verified by colony sequencing. Combinatorial libraries were ordered as IDT (Integrated DNA Technologies) ultramers with the final DNA diversity ranging from 1e6 to 1e7.

All libraries were amplified using Kapa HiFi Polymerase (Kapa Biosystems) with a qPCR machine (BioRAD CFX96). In detail, the libraries were firstly amplified in a 25 ul reaction, and PCR reaction was terminated when the reaction reached half the maximum yield to avoid over amplification. The PCR product was loaded to a DNA agarose gel. The band with the expected size was cut out and DNA fragments were extracted using QIAquick kits (Qiagen, Inc.). Then, the DNA product was re-amplified as before to generate enough DNA for yeast transformation. The final PCR product was cleaned up with a QIAquick Clean up kit (Qiagen, Inc.). For the yeast transformation, 2-3 µg of digested modified pETcon vector (pETcon3) and 6 µg of insert were transformed into EBY100 yeast strain using the protocol as described in (11).

DNA libraries for deep sequencing were prepared using the same PCR protocol, except the first step started from yeast plasmid prepared from 5×10^7 to 1×10^8 cells by Zymoprep (Zymo

Research). Illumina adapters and 6-bp pool-specific barcodes were added in the second qPCR step. Gel extraction was used to get the final DNA product for sequencing. All libraries include the native library and different sorting pools were sequenced using Illumina NextSeq/MiSeq sequencing.

Yeast surface display

S. cerevisiae EBY100 strain cultures were grown in C-Trp-Ura media and induced in SGCAA media following the protocol in (11). Cells were washed with PBSF (PBS with 1% BSA) and labelled with biotinylated RBD using two labeling methods, with-avidity and without-avidity labeling. For the with-avidity method, the cells were incubated with biotinylated RBD, together with anti-c-Myc fluorescein isothiocyanate (FITC, Miltenyi Biotec) and streptavidin–phycoerythrin (SAPE, ThermoFisher). The concentration of SAPE in the with-avidity method was used at ¼ concentration of the biotinylated RBD. The with-avidity method was used in the first few rounds of screening of the original design to fish out weak binder candidates. For the without-avidity method, the cells were firstly incubated with biotinylated RBD, washed, secondarily labelled with SAPE and FITC. For the ACE2 helix scaffolded designs, three rounds of with-avidity sorts were applied at 1 uM concentration of RBD. For the original library of de novo designs, the library was sorted twice using the with-avidity method at 1 uM RBD, followed by several without-avidity sort in the third round of sorting with RBD concentrations at 1uM, 100nM and 10 nM. The SSM library was screened using the without-avidity method for four rounds, with RBD concentrations at 1uM, 100nm, 10nM and 1nM. The error-prone library and the combinatorial libraries were sorted to convergence by decreasing the target concentration with each subsequent sort and collecting only the top 0.1% of the binding population. The final sorting pool of the error-prone library was sequenced using Illumina MiSeq kit to identify all beneficial mutations. The final sorting pools of the combinatorial libraries were plated on C-trp-ura plates and the sequences of individual clones were determined by Sanger sequencing.

For protease treatment, the cells were firstly washed with TBS (20 mM Tris 100 mM NaCl pH 8.0). Protolysis was initiated by adding 250 µL of room temperature TBS with 1 uM of trypsin and 0.5 uM of chymotrypsin, followed by vortexing and incubating the reaction at room temperature for 5 min. The reaction was quenched by adding 1 mL of chilled PBSF, and cells were immediately washed 4x in chilled PBSF. The cells were then labeled with RBD using the above mentioned protocol.

Protein expression

Genes encoding the designed protein sequences were synthesized and cloned into modified pET-29b(+) *E. coli* plasmid expression vectors (GenScript, N-terminal 8x His-tagged followed by a TEV cleavage site). For all the designed proteins, the sequence of the N-terminal tag used is MSHHHHHHHSENLYFQSGGG (unless otherwise noted), which is followed immediately by the sequence of the designed protein. Plasmids were then transformed into chemically competent *E. coli* Lemo21 cells (NEB). Protein expression was performed using the Studier autoinduction media supplemented with antibiotic, and grown overnight. The cells were harvested by spinning at 4,000xg for 10 min and then resuspended in lysis buffer (300 mM NaCl, 30 mM Tris-HCL, pH 8.0, with 0.25% CHAPS for cell assay samples) with DNase and protease inhibitor tablets. The cells were lysed with a QSONICA SONICATORS sonicator for 4 minutes total (2 minutes on time, 10 sec on-10 sec off) with an amplitude of 80%. Then the soluble fraction was clarified by centrifugation at 20,000g for 30 min. The soluble fraction was purified by Immobilized Metal Affinity Chromatography (Qiagen) followed by FPLC size-exclusion chromatography (Superdex 75 10/300 GL, GE Healthcare). All protein samples were

characterized with SDS-PAGE with the purity higher than 95%. Protein concentrations were determined by absorbance at 280 nm measured using a NanoDrop spectrophotometer (Thermo Scientific) using predicted extinction coefficients.

Circular dichroism

Far-ultraviolet CD measurements were carried out with an JASCO-1500 equipped with a temperature-controlled multi-cell holder. Wavelength scans were measured from 260 to 190 nm at 25, 95°C and again at 25°C after fast refolding (~5 min). Temperature melts monitored dichroism signal at 222 nm in steps of 2°C/minute with 30s of equilibration time. Wavelength scans and temperature melts were performed using 0.3 mg/ml protein in PBS buffer (20mM NaPO₄, 150mM NaCl, pH 7.4) with a 1 mm path-length cuvette.

Melting temperatures were determined fitting the data with a sigmoid curve equation. 7 out of the 9 designs retained more than half of the mean residue ellipticity values, which indicated the T_m values are greater than 95°C. T_m values of AHB1/2 and LCB2 were determined as the inflection point of the fitted function.

Biolayer interferometry

Biolayer interferometry binding data were collected in an Octet RED96 (ForteBio) and processed using the instrument's integrated software. For minibinder binding assays, biotinylated RBD (Acro Biosystems, for de novo miniprotein binders) or Fc tagged RBD (kindly provided by Erik Procko, for the ACE2 helix scaffolded binders), or Fc tagger SARS-CoV RBD (Sino Biological, for binding assay of AHB1, AHB2, LCB1 and LCB3) was loaded onto streptavidin-coated biosensors (SA ForteBio) or proteinA biosensors (ProteinA ForteBio) at 20 nM in binding buffer (10 mM HEPES (pH 7.4), 150 mM NaCl, 3 mM EDTA, 0.05% surfactant P20, 0.5% non-fat dry milk) for 360 s. Analyte proteins were diluted from concentrated stocks into binding buffer. After baseline measurement in the binding buffer alone, the binding kinetics were monitored by dipping the biosensors in wells containing the target protein at the indicated concentration (association step) and then dipping the sensors back into baseline/buffer (dissociation). For the ACE2 competition assay, ACE2-Fc protein (house made) was loaded onto proteinA biosensors (SA ForteBio) at 20 nM in binding buffer for 360 s, and the RBD protein (house made) was used as the ligand with a concentration of 100 nM. AHB1 protein was diluted into the ligand well at the indicated concentrations. Same Octet protocol as above mentioned was applied for acquiring the association and dissociation spectrums.

SARS-CoV-2 neutralization assay

SARS-CoV-2 strain 2019 n-CoV/USA_WA1/2020 was obtained from the Centers for Disease Control and Prevention (gift of Natalie Thornburg). Virus stocks were produced in Vero CCL81 cells (ATCC) and titrated by focus-forming assay on Vero E6 cells. Serial dilutions of minibinders were incubated with 10² focus-forming units (FFU) of SARS-CoV-2 for 1 h at 37°C. RBD binder-virus complexes were added to Vero E6 cell monolayers in 96-well plates and incubated for 1 h at 37°C. Next, cells were overlaid with 1% (w/v) methylcellulose in MEM supplemented to contain 2% FBS. Plates were harvested 30 h later by removing overlays and fixed with 4% PFA in PBS for 20 min at room temperature. Plates were washed and sequentially incubated with 1 µg/mL of CR3022 (5) anti-S antibody and HRP-conjugated goat anti-human IgG in PBS supplemented to contain 0.1% saponin and 0.1% BSA. SARS-CoV-2-infected cell

foci were visualized using TrueBlue peroxidase substrate (KPL) and quantitated on an ImmunoSpot microanalyzer (Cellular Technologies). Data was processed using Prism software (GraphPad Prism 8.0).

Cryo Electron microscopy

To prepare SARS-CoV-2 S/LCB complexes, 10-fold molar excesses of LCB1 or LCB3 were incubated with SARS-CoV-2 HexaPro Spike protein (21) for 1 h on ice, and the complexes were purified on a Superose 6 Increase 10/300 GL column. 3 μ L of 1 mg/ml purified SARS-CoV S/LCB complexes were loaded onto a freshly glow-discharged (30 s at 20 mA) 1.2/1.3 UltrAuFoil grid (300 mesh) prior to plunge freezing using a vitrobot Mark IV (ThermoFisher Scientific) using a blot force of 0 and 5.5 second blot time at 100% humidity and 25°C. Data were acquired using an FEI Titan Krios transmission electron microscope operated at 300 kV and equipped with a Gatan K2 Summit direct detector and Gatan Quantum GIF energy filter, operated in zero-loss mode with a slit width of 20 eV. Automated data collection was carried out using Leginon (22) at a nominal magnification of 130,000x with a pixel size of 0.525 Å. The dose rate was adjusted to 8 counts/pixel/s, and each movie was acquired in super-resolution mode fractionated in 50 frames of 200 ms. 2,500 micrographs were collected with a defocus range between -0.5 and -2.5 μ m. Movie frame alignment, estimation of the microscope contrast-transfer function parameters, particle picking, and extraction were carried out using Warp (23). Particle images were extracted with a box size of 800 binned to 400 yielding a pixel size of 1.05 Å. Reference-free 2D classification was performed using CryoSPARC (24) to select well-defined particle images. These selected particles were subjected to 3D classification in Relion (25, 26). 3D refinements were carried out using non-uniform refinement along with per-particle defocus refinement in CryoSPARC (27). Selected particle images were subjected to the Bayesian polishing procedure implemented in Relion3.0 (28). After non-uniform refinement in cryoSPARC, the particles were then subjected to focus 3D classification without refining angles and shifts using a soft mask on Receptor binding motif (RBM) and LCB region with a tau value of 60 in Relion. Particles belonging to classes with the best resolved LCB1/3 density were selected and subject to local refinement with CryoSPARC, resulting in 3D reconstructions with improved quality for the minibinders. Local resolution estimation, filtering, and sharpening were carried out using CryoSPARC. Reported resolutions are based on the gold-standard Fourier shell correlation (FSC) of 0.143 criterion and Fourier shell correlation curves were corrected for the effects of soft masking by high-resolution noise substitution (29).

CryoEM model building and analysis.

UCSF Chimera (30) and Coot (31) were used to fit atomic models (PDB 6VXX or PDB 6VYB) into the cryoEM maps and the LCB1 or LCB3 designed models. Models were refined and relaxed using Rosetta using both sharpened and unsharpened maps (32-34) and validated using Molprobit (35), Phenix (36), Privateer (37) and EMRinger (38). Figures were generated using UCSF ChimeraX (39).

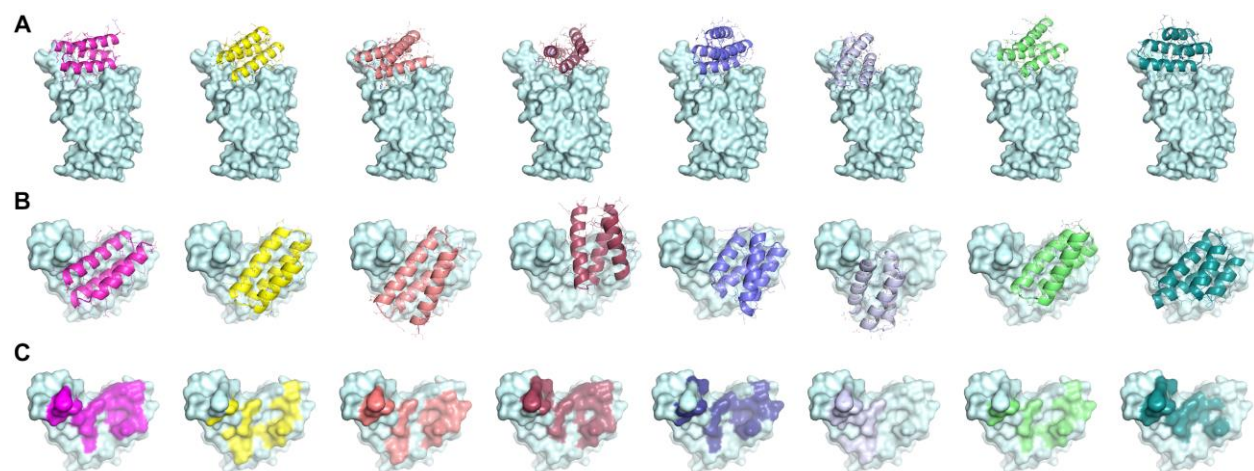


Figure S1 | Gallery of *de novo designed* miniprotein binders that bind to SARS-CoV-2 RBD with different binding configurations. Side views of *de novo* miniprotein binder-RBD complexes (LCB1-8) are shown in (A) and top views are shown in (B). (C) Residues on RBD that are within 8Å C β distance are highlighted.

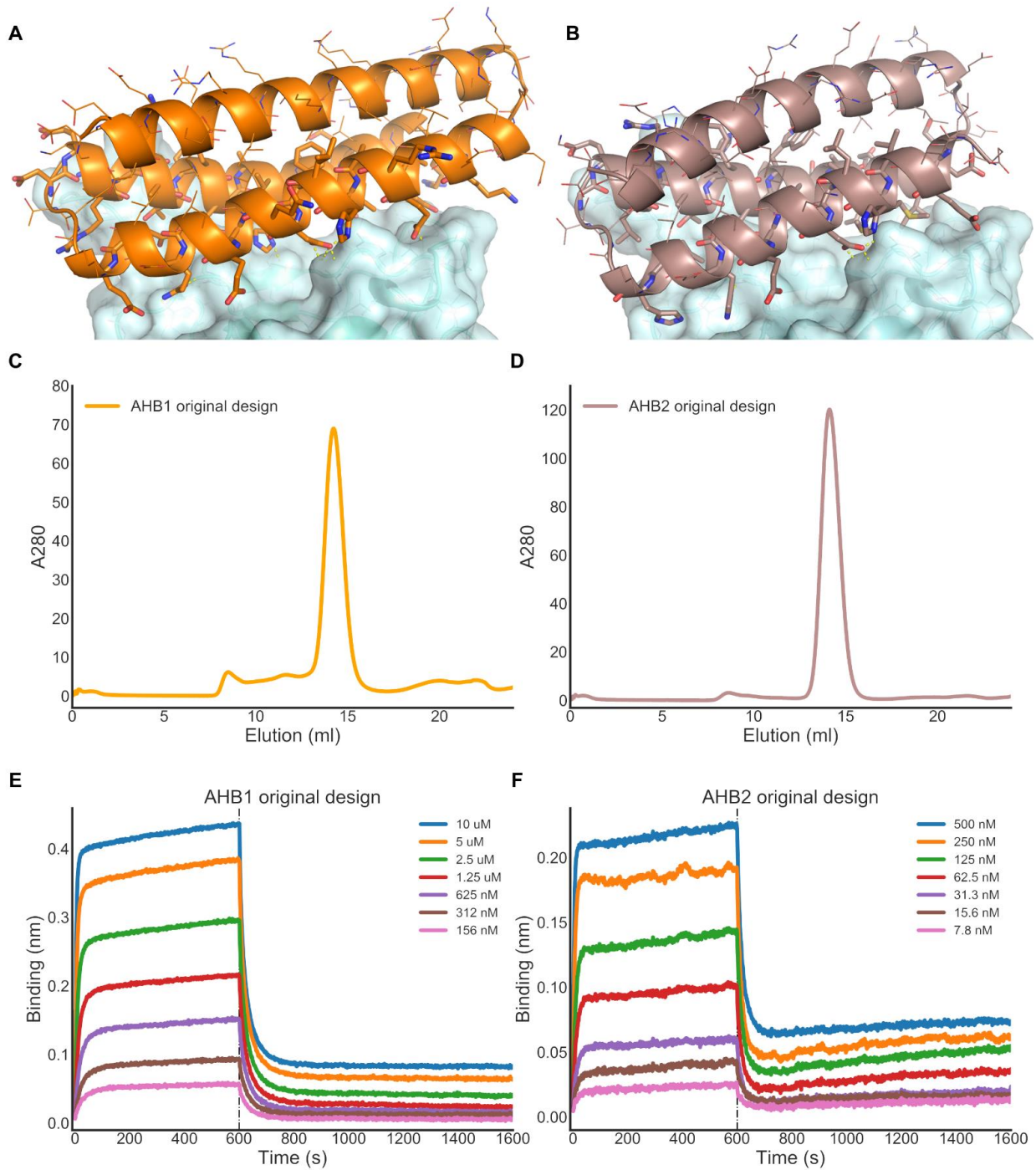


Figure S2 | Expression and characterization of ACE2 scaffolded design. (A) and (B) Design model of the identified ACE2 scaffolded design in complex with RBD. (C) and (D) Size Exclusion chromatography profile of the E. coli expressed protein. (E) and (F) Binding of ACE2 scaffolded design to RBD in the biolayer interferometry experiments. Fc-tagged RBD protein was loaded onto Protein A biosensors, and allowed to equilibrate before setting the baseline to

zero at $t=0$. The BLI tips were then placed into different concentrations of AHB1 as indicated for 600 seconds. The tips were then placed into buffer solution and the dissociation was monitored for an additional 1,000 seconds.

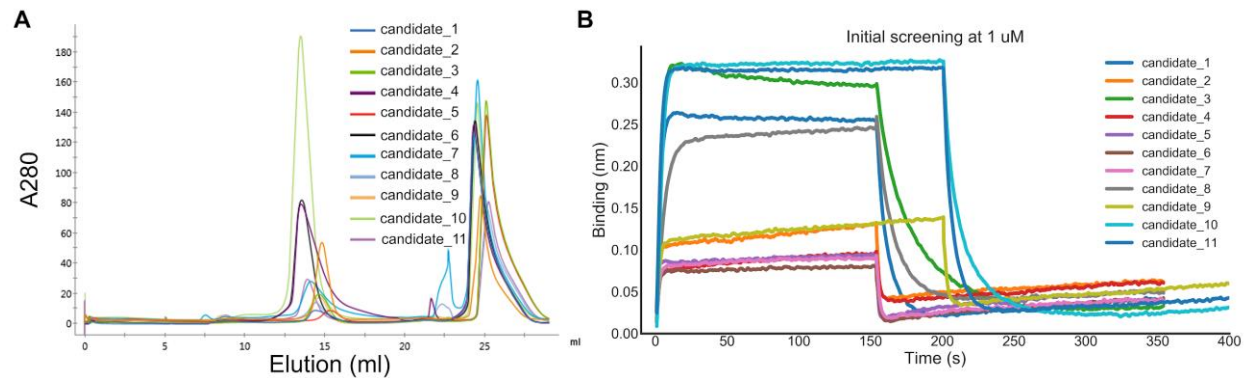


Figure S3 | Expression and characterization of *de novo* designed miniprotein binders. (A) Size Exclusion chromatography profiles of the *E. coli* expressed initial hits by the *de novo* approach. (B) Binding profiles of *de novo* miniproteins to RBD in the biolayer interferometry experiments. The biotinylated RBD protein was loaded onto the Streptavidin (SA) biosensors and allowed to equilibrate before setting the baseline to zero at $t=0$. The BLI tips were then placed into different concentrations of candidate minibinders (1 uM) as indicated for 150-200 seconds. The tips were then placed into buffer solution and the dissociation was monitored for an additional 600 seconds.

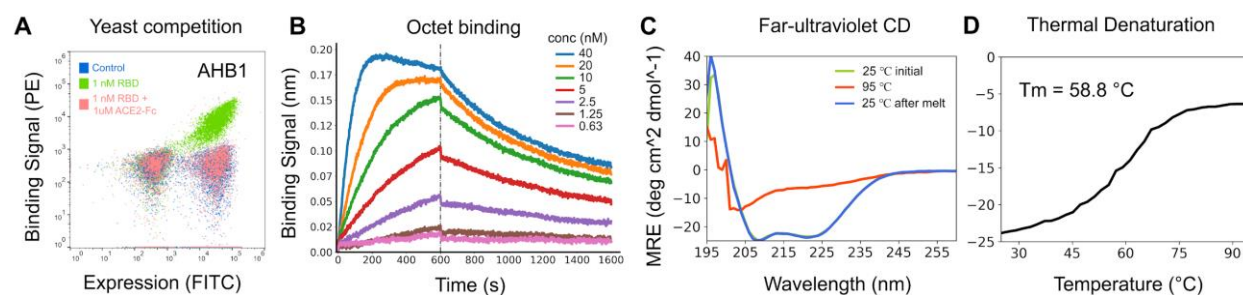


Figure S4 | The optimized design AHB1 binds with high affinity to the RBD, competes with ACE2, and is not super thermostable. A. ACE2 competes with the designs for binding to the RBD. Yeast cells displaying the indicated design were incubated with 1nM RBD in the presence or absence of 1 μ M ACE2, and RBD binding to cells (Y axis) was monitored by flow cytometry. B. Binding of purified miniproteins to the RBD monitored by biolayer interferometry. The biotinylated RBD protein was loaded onto the Streptavidin (SA) biosensors and allowed to equilibrate before setting the baseline to zero at t=0. The BLI tips were then placed into different concentrations of candidate minibinders (at concentrations noted) as indicated for 600 seconds. The tips were then placed into buffer solution and the dissociation was monitored for an additional 1,000 seconds. C. Circular dichroism (CD) spectra at different temperatures, and D. CD signal at 222 nm wavelength as a function of temperature.

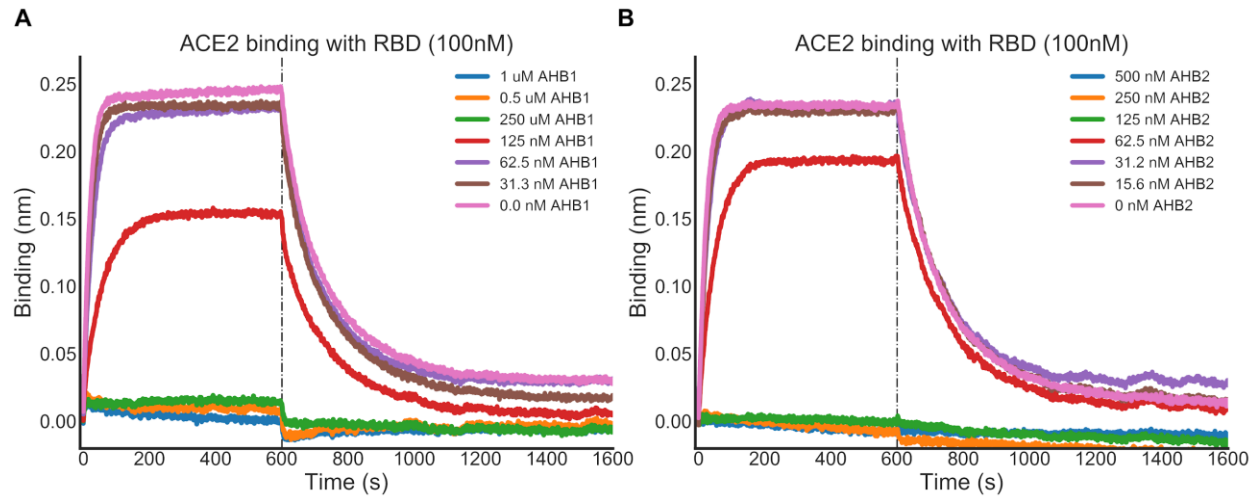


Figure S5 | The ACE2 scaffolded helix design AHB1/2 blocks binding of ACE2 to the RBD. The Fc-tagged ACE2 protein was loaded onto the Protein A biosensors in the BLI assay, and allowed to equilibrate before setting the baseline to zero at $t=0$. The BLI tips were then placed for 600 seconds into different concentrations of AHB1 (A) and AHB2 (B) minibinder as indicated, together with a constant concentration of 100 nM of RBD. The tips were then placed into buffer solution and the dissociation was monitored for an additional 1000 seconds.

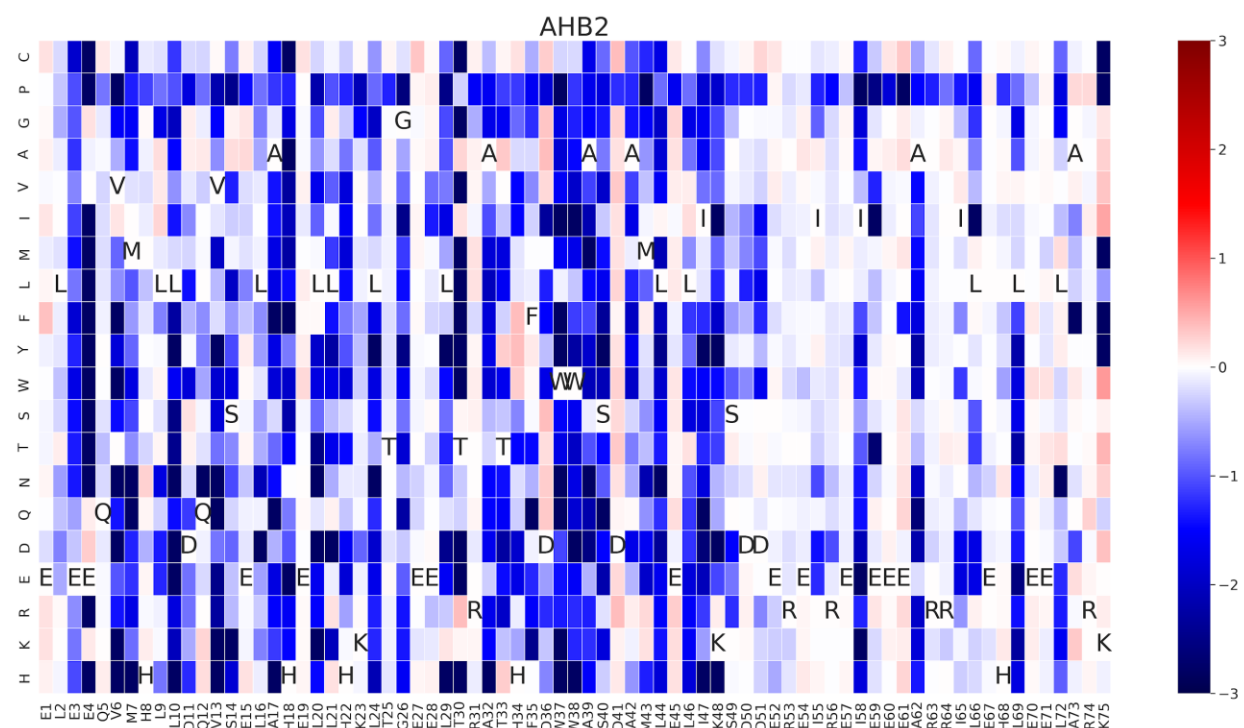
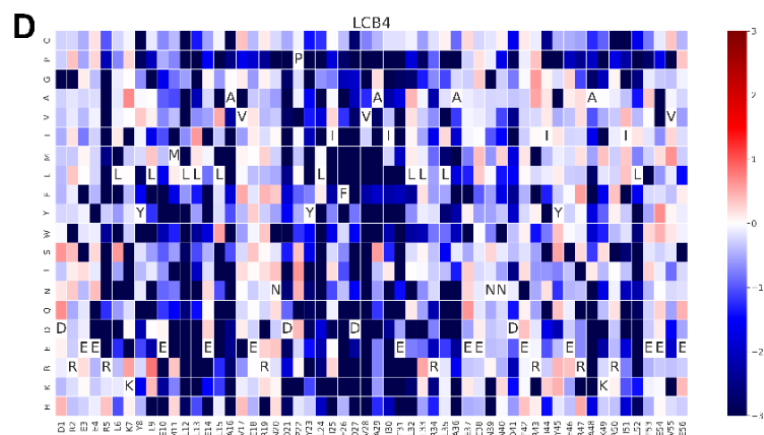
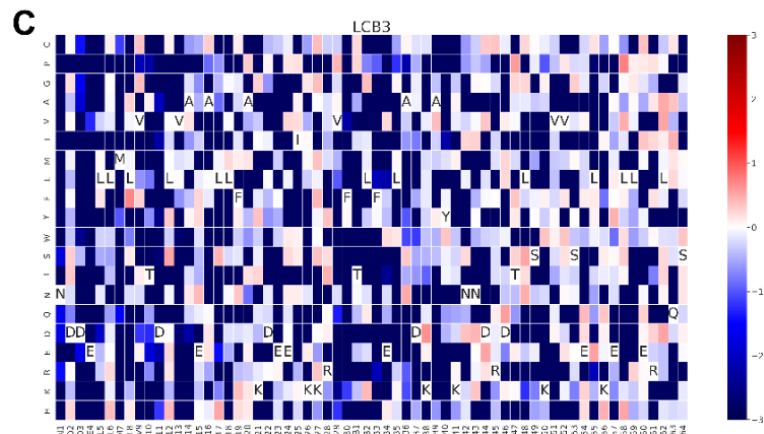
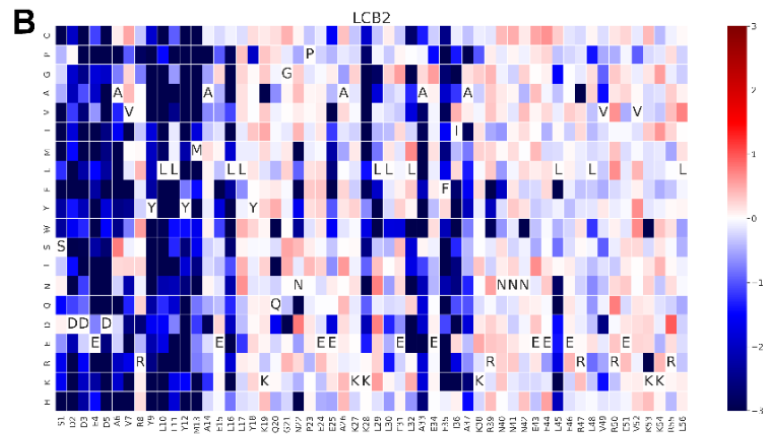
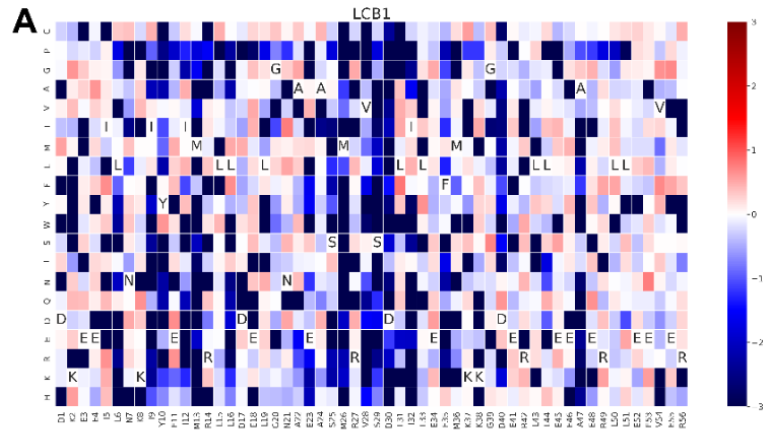


Figure S6 | SSM maps for the parent design of AHB2. Colors indicate relative enrichment or depletion of a substitution relative to the unselected population.



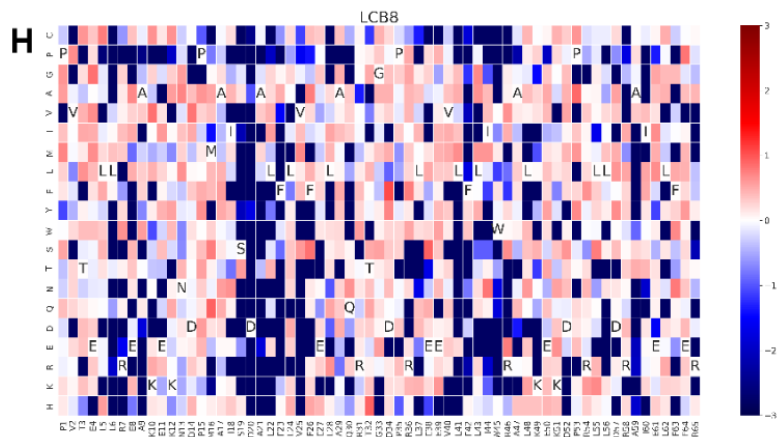
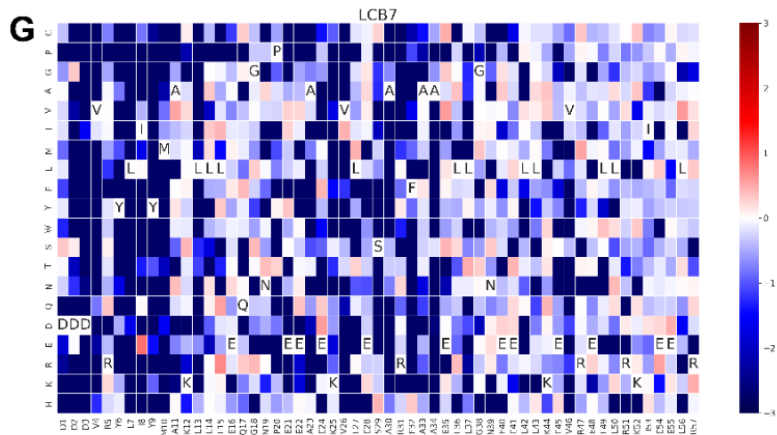
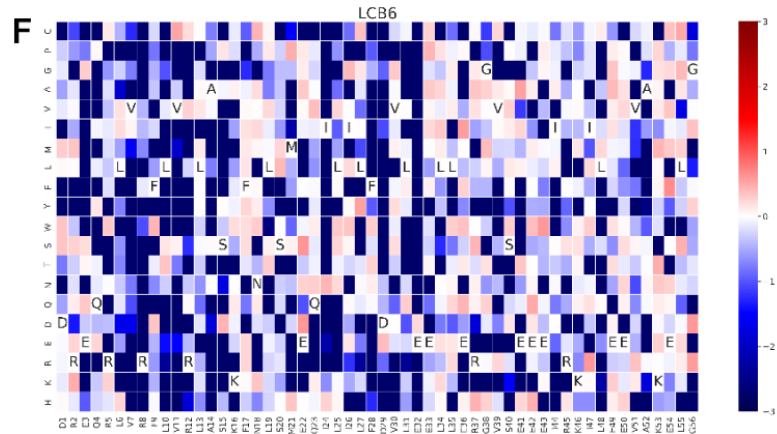
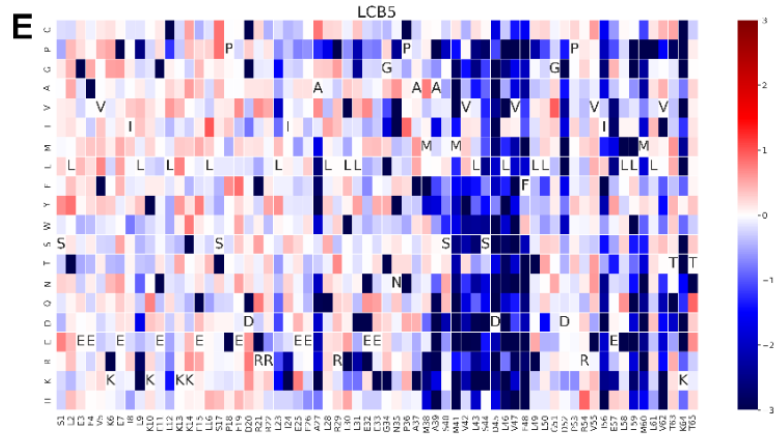


Figure S7 | SSM maps for all eight de novo miniprotein binders. Colors indicate relative enrichment or depletion of a substitution relative to the unselected population.

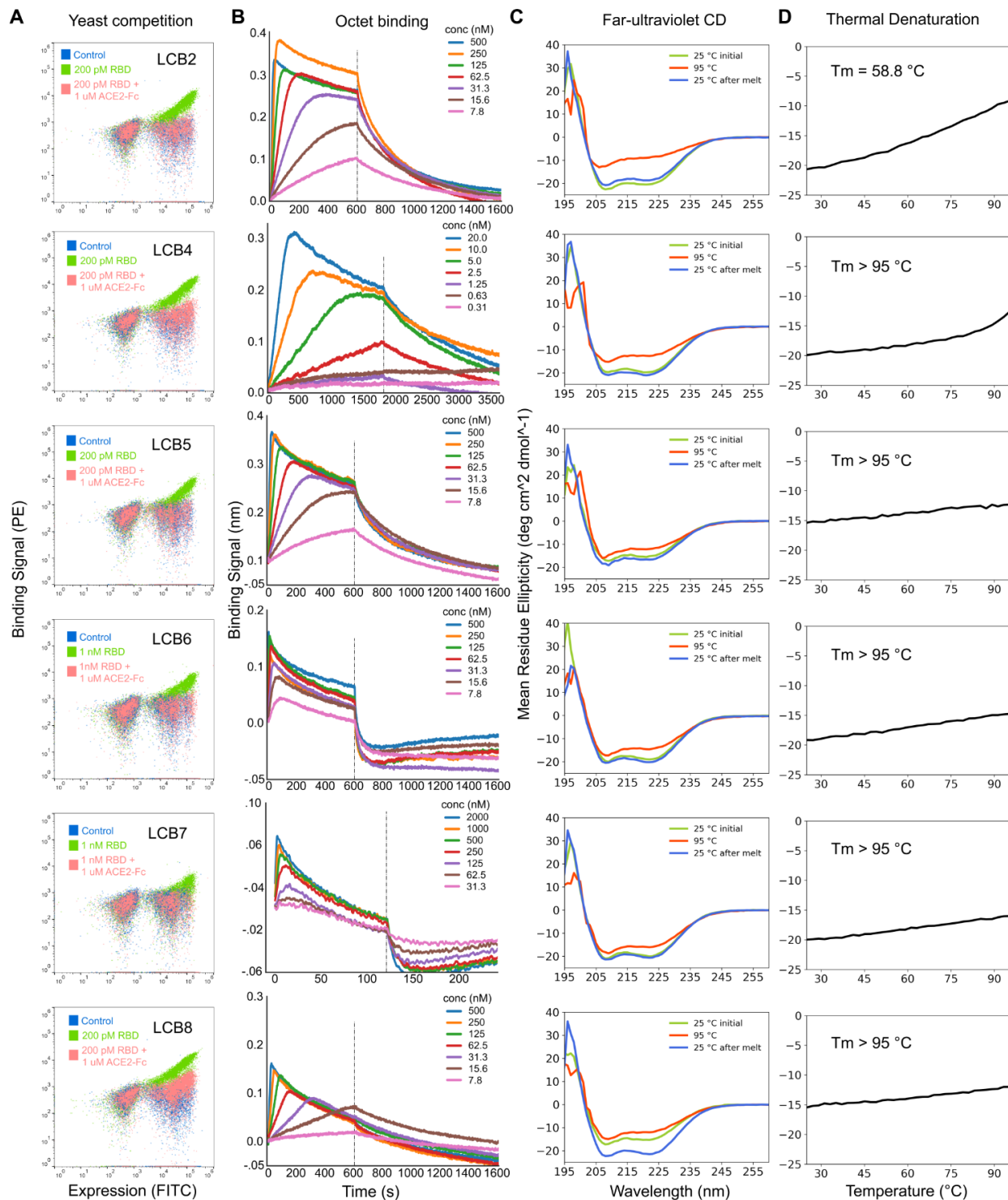


Figure S8 | The optimized designs bind with high affinity to the RBD, compete with ACE2, and are thermostable. A. ACE2 competes with the designs for binding to the RBD. Yeast cells displaying the indicated design were incubated with 1nM/200pM RBD in the presence or absence of 1uM ACE2, and RBD binding to cells (Y axis) was monitored by flow cytometry. B. Binding of purified miniproteins to the RBD monitored by biolayer interferometry. The biotinylated RBD protein was loaded onto the Streptavidin (SA) biosensors and allowed to

equilibrate before setting the baseline to zero at $t=0$. The BLI tips were then placed into different concentrations of candidate minibinders (at concentrations noted) as indicated for 120 or 600 seconds. The tips were then placed into buffer solution and the dissociation was monitored for an additional 300 or 1,000 seconds. C. Circular dichroism (CD) spectra at different temperatures, and D. CD signal at 222 nm wavelength as a function of temperature.

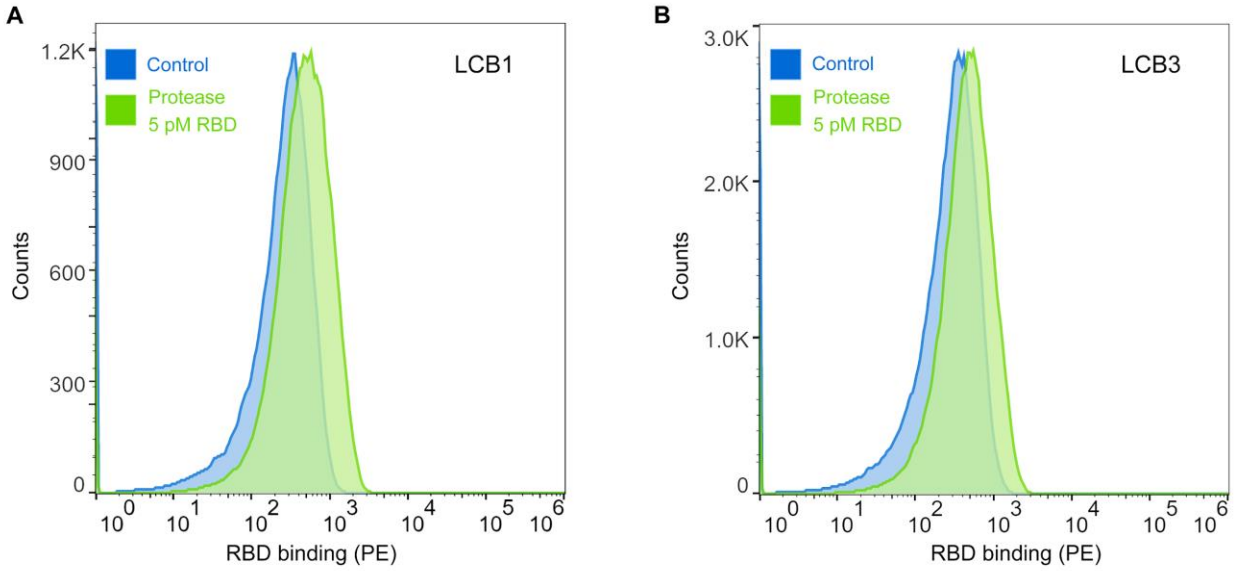


Figure S9 | LCB1 and LCB3 bind to RBD at 5 pM following protease treatment. Yeast cells displaying LCB1 (A) and LCB3 (B) were incubated with 1uM trypsin and 0.5 uM chymotrypsin, washed, incubated with 5 pM biotinylated RBD, and analyzed by flow cytometry.

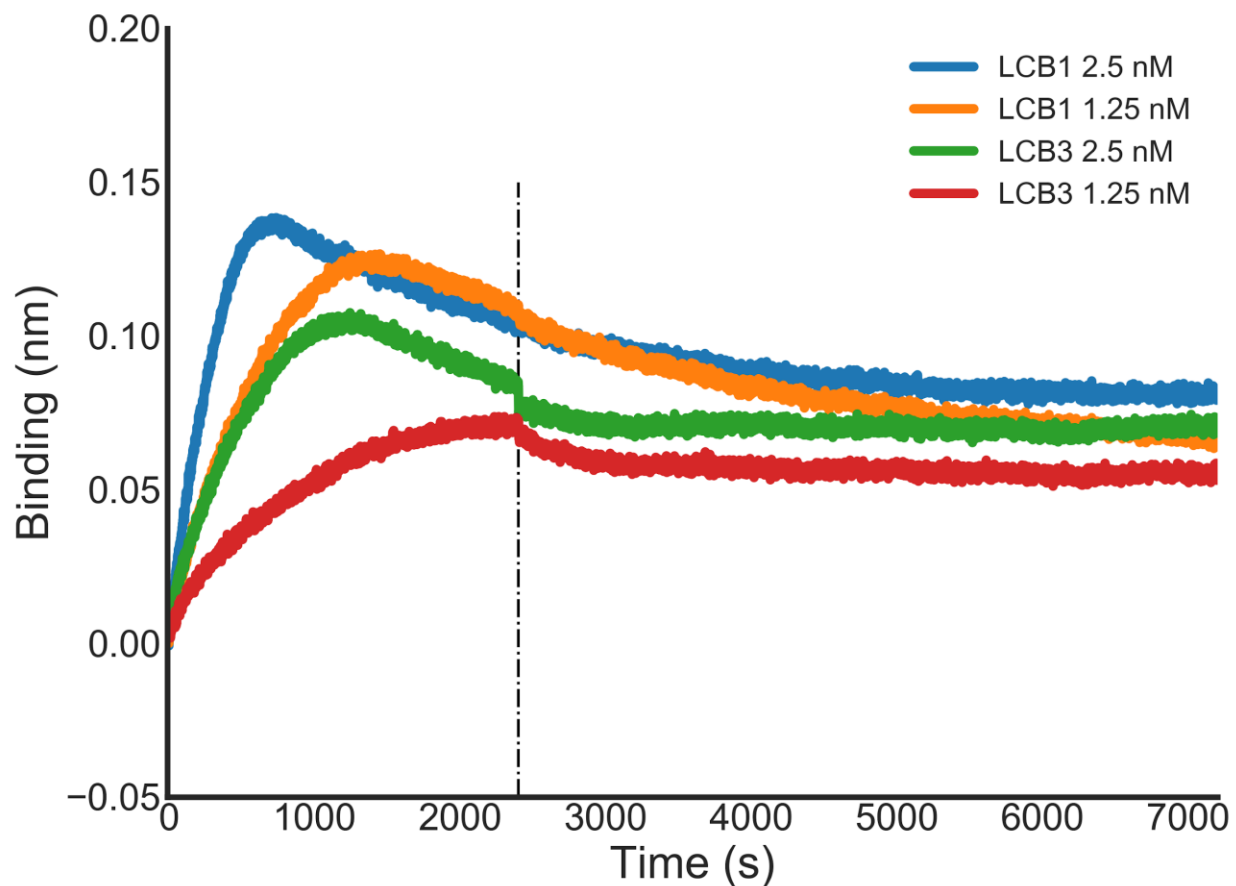


Figure S10 | LCB1 and LCB3 retain activity after a few days at room temperature. LCB1 and LCB3 were left on the lab bench at room temperature for 14 days and the binding with RBD was checked using the BLI assay. Fc-tagged RBD protein was loaded onto Protein A biosensors, and allowed to equilibrate before setting the baseline to zero at $t=0$. The BLI tips were then placed into different concentrations LCB1 and LCB3 as indicated for 2500 seconds. The tips were then placed into buffer, and the dissociation was monitored for an additional 4500 seconds.

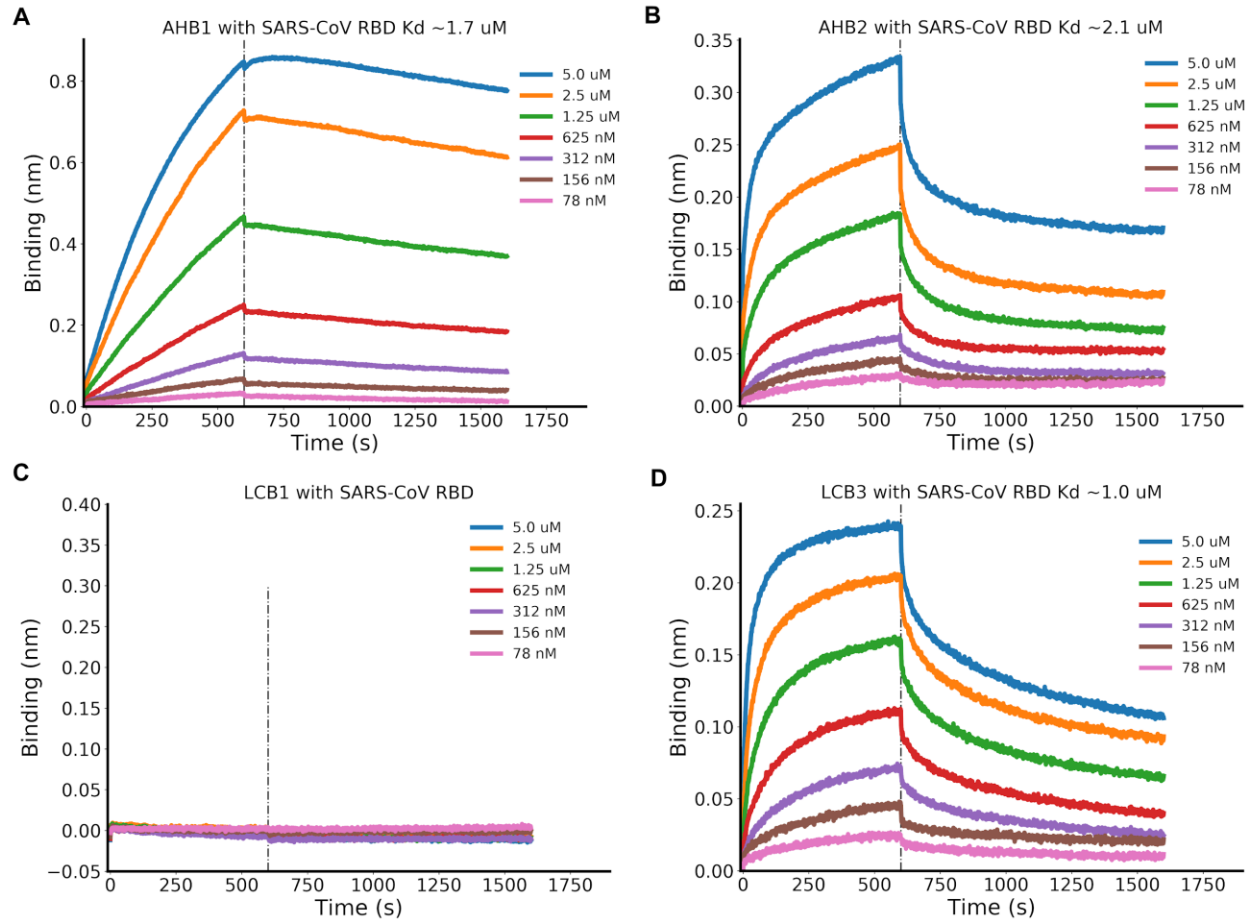


Figure S11 | AHB1, AHB2 and LCB3, but not LCB1, show cross reactivity with SARS-CoV RBD. For the BLI assay, the Fc-tagged SARS-CoV RBD protein was loaded onto Protein A biosensors, and allowed to equilibrate before setting the baseline to zero at t=0. The BLI tips were then placed into different concentrations of AHB1 (A), AHB2 (B), LCB1 (C) and LCB3 (D) as indicated for 600 seconds. The tips were then placed into buffer, and the dissociation was monitored for an additional 1000 seconds.

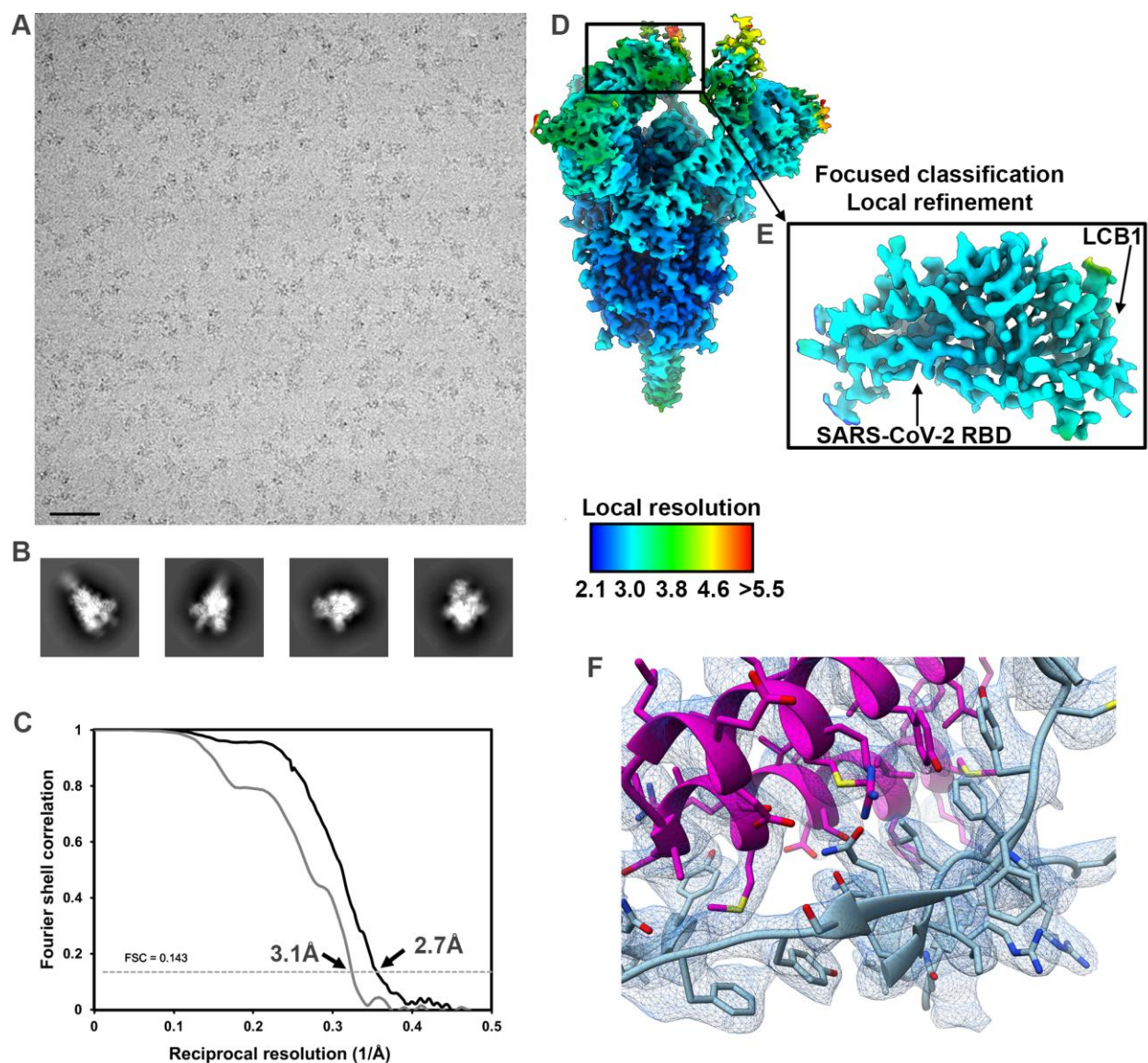


Figure S12 | CryoEM data processing and validation of the SARS-CoV-2 structure in complex with LCB1. **A-B.** Representative electron micrograph (A) and 2D class averages (B) of SARS-CoV-2 S in complex with LCB1 embedded in vitreous ice. Scale bar: 400Å. **C.** Gold-standard Fourier shell correlation curves for the LCB1-bound trimer (black solid line) and locally refined RBD/LCB1 (grey solid line). The 0.143 cutoff is indicated by horizontal dashed lines. **D-E.** Local resolution maps calculated using cryoSPARC for LCB1/S (D) and the locally refined RBD/LCB1 region (E). **F.** Zoomed-in view of the interface between LCB1 (magenta) and the SARS-CoV-2 RBD (cyan) with the corresponding region of density shown as blue mesh.

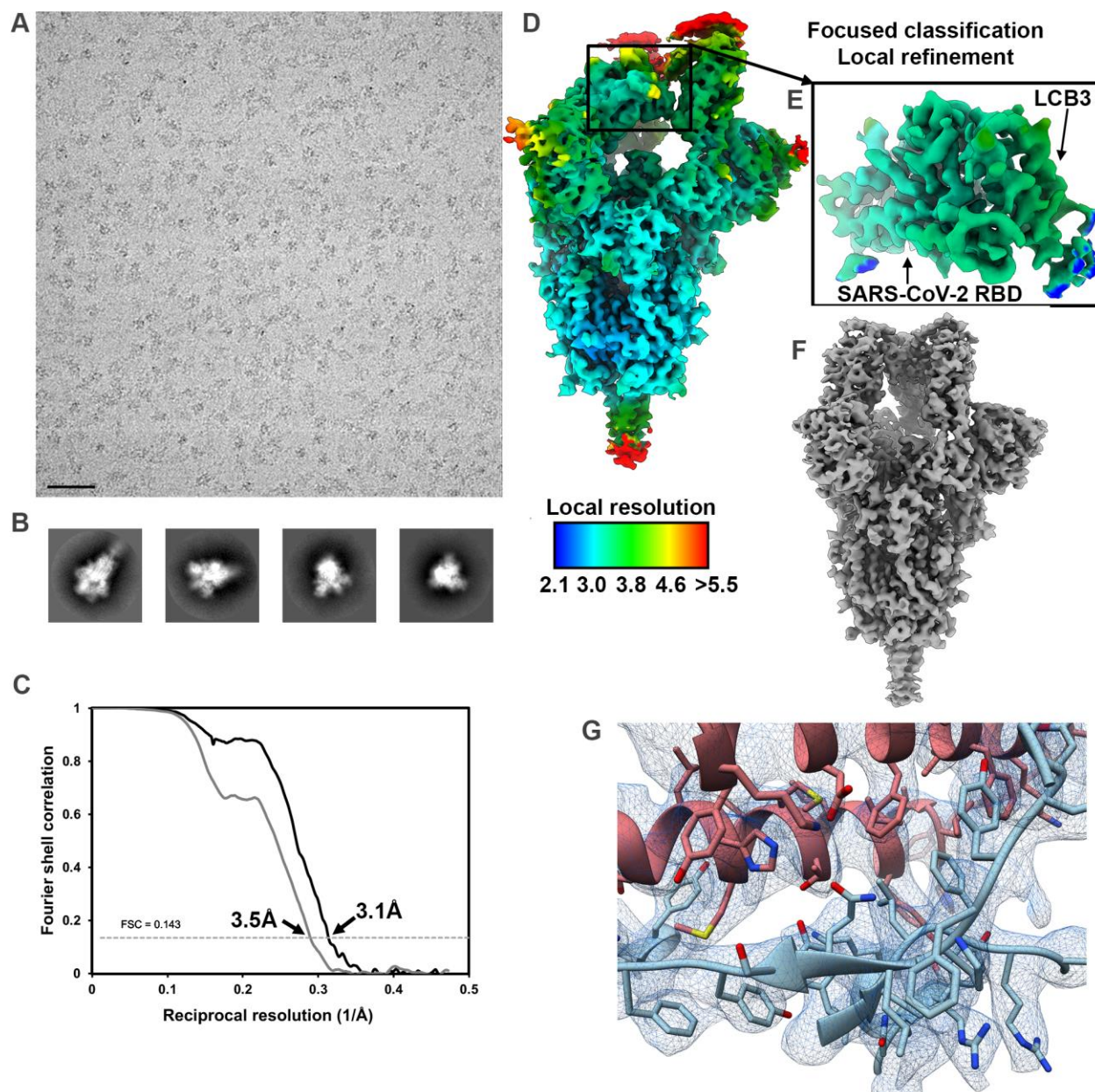


Figure S13 | CryoEM data processing and validation of the SARS-CoV-2 structure in complex with LCB3. **A-B.** Representative electron micrograph (A) and 2D class averages (B) of SARS-CoV-2 S in complex with LCB3 embedded in vitreous ice. Scale bar: 400Å. **C.** Gold-standard Fourier shell correlation curves for the LCB3-bound trimer (black solid line) and locally refined RBD/LCB3 (grey solid line). The 0.143 cutoff is indicated by horizontal dashed lines. **D-E.** Local resolution maps calculated using cryoSPARC for LCB3/S (D) and the locally refined RBD/LCB3 region (E). **F.** CryoEM reconstruction of LCB3 in complex with SARS-CoV-2 S with three RBDs open. **G.** Zoomed-in view of the interface between LCB3 (salmon) and the SARS-CoV-2 RBD (cyan) with the corresponding region of density shown as blue mesh.

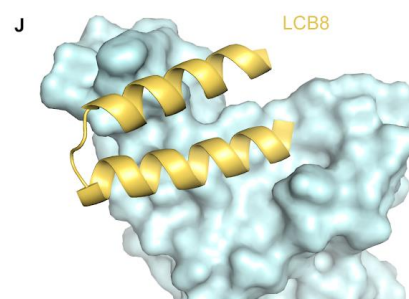
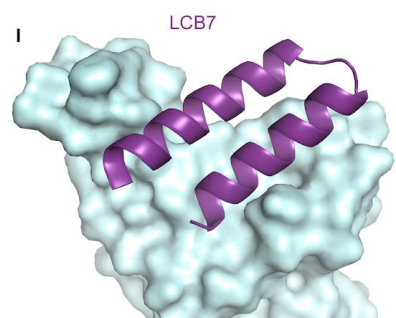
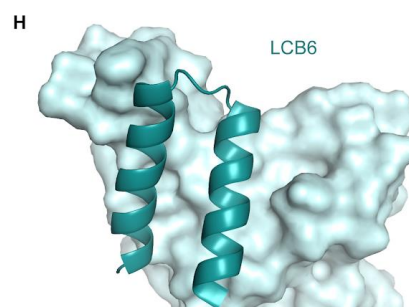
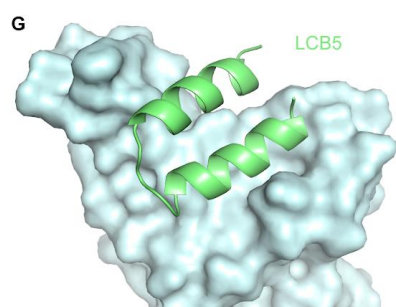
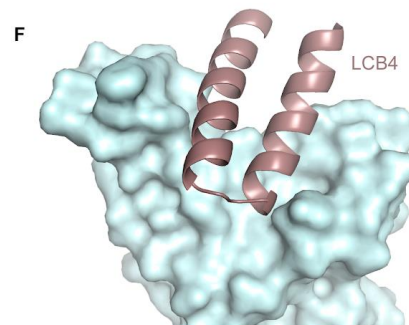
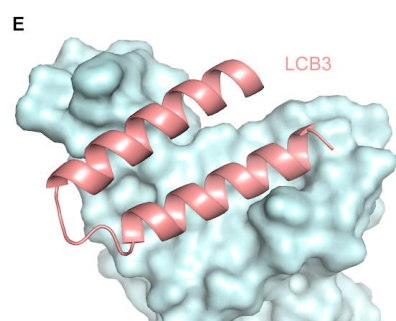
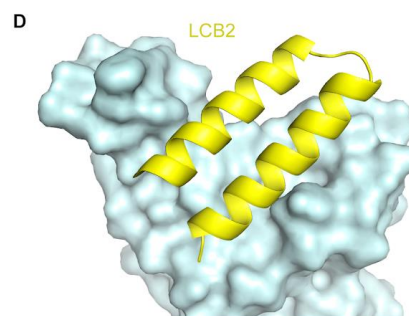
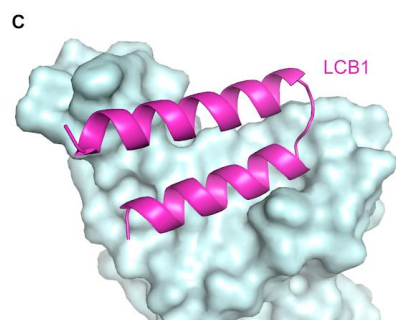
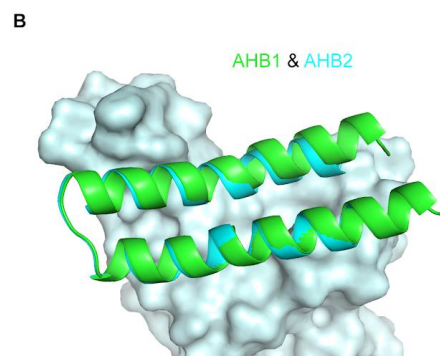
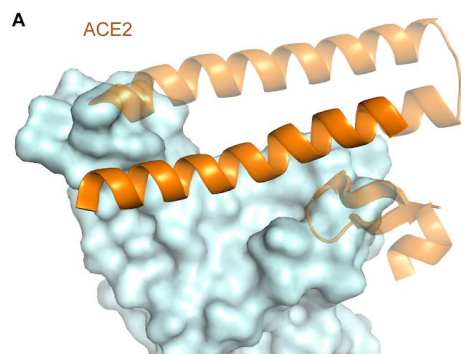


Figure S14 | The main binding elements of the *de novo* binders overlap with ACE2, which explains the competitive binding with ACE2 and their neutralization activities. A. The interface elements of ACE2 binding with RBD (shown as surface in cyan) are shown in brown and the main binding helix which is used in Approach 1 is highlighted. The interface helix hairpin of the *de novo* binders are shown in B-J. Design models are used for AHB1, AHB2, LCB2 and LCB4-8, whereas the CryoEM structures of LCB1 and LCB3 are used to generate the figures.

Table S1 Residues on RBD making contacts with ACE2 and the *de novo* binders (indices are according to PDB 6M0J). All the interaction residues that have a binding energy (Rosetta ΔG upon binding) smaller than zero are included.

name	Interface residues
ACE2	417K,421Y,445V,446G,449Y,453Y,455L,456F,473Y,474Q,475A,476G,484E,485G,486F,487N,488C,489Y,491P,492L,493Q,494S,497F,498Q,499P,500T,501N,502G,503V,505Y
AHB1	403R,406E,408R,409Q,415T,416G,417K,421Y,444K,445V,446G,447G,448N,449Y,453Y,454R,455L,456F,457R,460N,473Y,474Q,475A,476G,484E,486F,487N,488C,489Y,492L,493Q,494S,496G,498Q,500T,501N,502G,504G,505Y
AHB2	403R,408R,415T,416G,417K,419A,420D,421Y,446G,449Y,453Y,455L,456F,457R,458K,460N,473Y,475A,476G,478T,484E,486F,487N,489Y,490F,492L,493Q,494S,495Y,496G,497F,498Q,501N,502G,503V,504G,505Y
LCB1	402I,404G,408R,414Q,415T,416G,420D,445V,448N,454R,455L,459S,473Y,474Q,475A,476G,477S,483V,485G,486F,487N,488C,490F,492L,494S,495Y,496G,497F,499P,500T,501N,504G,505Y,506Q
LCB2	403R,405D,408R,409Q,416G,417K,418I,420D,421Y,446G,447G,453Y,455L,456F,458K,474Q,475A,476G,484E,487N,488C,489Y,490F,492L,493Q,494S,495Y,496G,497F,498Q,499P,500T,501N,502G,505Y
LCB3	402I,407V,408R,415T,416G,417K,418I,419A,420D,446G,448N,452L,453Y,454R,455L,456F,459S,472I,473Y,474Q,475A,476G,483V,485G,486F,487N,488C,489Y,492L,494S,495Y,496G,497F,500T,501N,504G,505Y,506Q
LCB4	403R,405D,406E,417K,444K,446G,447G,448N,449Y,453Y,455L,456F,483V,484E,485G,486F,487N,488C,489Y,492L,493Q,495Y,496G,497F,498Q,499P,500T,501N,502G,504G,505Y
LCB5	403R,408R,415T,416G,417K,418I,420D,421Y,446G,447G,449Y,453Y,455L,456F,460N,473Y,486F,487N,488C,489Y,490F,491P,492L,493Q,494S,495Y,496G,497F,498Q,501N,504G,505Y,506Q,507P
LCB6	403R,408R,409Q,415T,416G,417K,418I,419A,421Y,453Y,455L,456F,457R,458K,459S,473Y,474Q,475A,476G,477S,484E,486F,487N,488C,489Y,493Q,494S,496G,505Y
LCB7	403R,405D,406E,408R,416G,417K,418I,421Y,446G,447G,449Y,453Y,455L,456F,473Y,475A,476G,484E,485G,486F,487N,488C,489Y,493Q,495Y,496G,497F,498Q,500T,501N,502G,504G,505Y,506Q
LCB8	403R,405D,406E,416G,417K,421Y,447G,449Y,453Y,454R,455L,456F,457R,458K,460N,472I,473Y,475A,476G,477S,484E,485G,486F,487N,489Y,491P,492L,493Q,494S,495Y,496G,498Q,501N,502G,504G,505Y

Table S2 The sequences of all biochemically characterized proteins.

name	sequence
AHB1	DEDEELERLYRKAEEVAKEAKDASRRGDDERAKEQMERAMRLFDQVFELAQELQEKQTDGNRQKATHLKD KAVKE AADELYQRVR
AHB2	ELEEQVMHVL DQVSELAHELLHKLTGEELERAAYFNWWATEMMLELIKSDDEREIREIEEEEARRILEHLEELARK
LCB1	DKEWILQKIYEIMRLLDELGHAEASMRVSDLIYEFMKKGDERLLEEAERLLEEVEER
LCB2	SDDEDSVRYLLYMAELRYEQGNPEKAKKILEMAEFI AKRNNNEELERLVREVKKRL
LCB3	NDDELHMLMTDLVYEALHFAKDEEIKKRVFQLFELADKAYKNDRQKLEKVVEELKELLERLLS
LCB4	QREKRLKQLEMLLEYAIERNDPYLMFDVAVEMLR LAEENNDERIIERAKRILEEYE
LCB5	SLEELKEQVKELKKELSP EMRR LIEEALRFLEEGNPAMAMMVLSDLVYQLGDPRVIDLYMLVTKT
LCB6	DREQRLVRFLVRLASKFNLSPEQILQLFEVLEELLERGVSEEEIRKQLEEVAKELG
LCB7	DDDIRYLIYMAKLRLEQGNPEEA EKVLEMARFLAERLGMEELLKEVRELLRKIEELR
LCB8	PIIELLREAKEKNDEFAISDALYLVNELLQRTGDPRLEEVL YLIWRALKEKDPRLLDRAIELFER

Table S3. CryoEM data collection and refinement statistics.

	SARS-CoV-2 S/LCB1 PDB-7JZL EMD-22532	SARS-CoV-2 S/LCB1 (local refinement) PDB-7JZU EMD-22574	SARS-CoV-2 S/LCB3 EMD-22534	SARS-CoV-2 S/LCB3 (local refinement) PDB-7JZM EMD-22533	SARS-CoV-2 S/LCB3 (3RBDs open) EMD-22535
Data collection and processing					
Magnification	130,000	130,000	130,000	130,000	130,000
Voltage (kV)	300	300	300	300	300
Electron exposure (e-/Å ²)	70	70	70	70	70
Defocus range (µm)	0.5-2.5	0.5-2.5	0.5-2.5	0.5-2.5	0.5-2.5
Pixel size (Å)	0.525	0.525	0.525	0.525	0.525
Symmetry imposed	C1	C1	C1	C1	C1
Final particle images (no.)	194,375	194,375	96,381	96,381	64,285
Map resolution (Å)	2.7	3.1	3.1	3.5	3.2
FSC threshold	0.143	0.143	0.143	0.143	0.143
Map sharpening <i>B</i> factor (Å ²)	-55	-58	-54	-56	-47

Validation					
MolProbity score	0.88	0.88	0.82	0.74	
Clashscore	0.54	0.52	0.36	0.76	
Poor rotamers (%)	0.34	0.5	0.16	0	
Ramachandran plot					
Favored (%)	96.8	96.7	97.6	98.0	
Allowed (%)	3.0	3.3	2.3	2.0	
Disallowed (%)	0.2	0	0.1	0	

References and Notes

1. Y. J. Hou, K. Okuda, C. E. Edwards, D. R. Martinez, T. Asakura, K. H. Dinno 3rd, T. Kato, R. E. Lee, B. L. Yount, T. M. Mascenik, G. Chen, K. N. Olivier, A. Ghio, L. V. Tse, S. R. Leist, L. E. Gralinski, A. Schäfer, H. Dang, R. Gilmore, S. Nakano, L. Sun, M. L. Fulcher, A. Livraghi-Butrico, N. I. Nicely, M. Cameron, C. Cameron, D. J. Kelvin, A. de Silva, D. M. Margolis, A. Markmann, L. Bartelt, R. Zumwalt, F. J. Martinez, S. P. Salvatore, A. Borczuk, P. R. Tata, V. Sontake, A. Kimple, I. Jaspers, W. K. O’Neal, S. H. Randell, R. C. Boucher, R. S. Baric, SARS-CoV-2 Reverse Genetics Reveals a Variable Infection Gradient in the Respiratory Tract. *Cell* **182**, 429–446.e14 (2020). [doi:10.1016/j.cell.2020.05.042](https://doi.org/10.1016/j.cell.2020.05.042) [Medline](#)
2. R. Shi, C. Shan, X. Duan, Z. Chen, P. Liu, J. Song, T. Song, X. Bi, C. Han, L. Wu, G. Gao, X. Hu, Y. Zhang, Z. Tong, W. Huang, W. J. Liu, G. Wu, B. Zhang, L. Wang, J. Qi, H. Feng, F. S. Wang, Q. Wang, G. F. Gao, Z. Yuan, J. Yan, A human neutralizing antibody targets the receptor-binding site of SARS-CoV-2. *Nature* **584**, 120–124 (2020). [doi:10.1038/s41586-020-2381-y](https://doi.org/10.1038/s41586-020-2381-y) [Medline](#)
3. D. Pinto, Y.-J. Park, M. Beltramello, A. C. Walls, M. A. Tortorici, S. Bianchi, S. Jaconi, K. Culap, F. Zatta, A. De Marco, A. Peter, B. Guarino, R. Spreafico, E. Camerini, J. B. Case, R. E. Chen, C. Havenar-Daughton, G. Snell, A. Telenti, H. W. Virgin, A. Lanzavecchia, M. S. Diamond, K. Fink, D. Veelsler, D. Corti, Structural and functional analysis of a potent sarbecovirus neutralizing antibody. *bioRxiv* 023903 [Preprint] 10 April 2020; <https://doi.org/10.1101/2020.04.07.023903>.
4. J. Lan, J. Ge, J. Yu, S. Shan, H. Zhou, S. Fan, Q. Zhang, X. Shi, Q. Wang, L. Zhang, X. Wang, Structure of the SARS-CoV-2 spike receptor-binding domain bound to the ACE2 receptor. *Nature* **581**, 215–220 (2020). [doi:10.1038/s41586-020-2180-5](https://doi.org/10.1038/s41586-020-2180-5) [Medline](#)
5. M. Yuan, N. C. Wu, X. Zhu, C. D. Lee, R. T. Y. So, H. Lv, C. K. P. Mok, I. A. Wilson, A highly conserved cryptic epitope in the receptor binding domains of SARS-CoV-2 and SARS-CoV. *Science* **368**, 630–633 (2020). [doi:10.1126/science.abb7269](https://doi.org/10.1126/science.abb7269) [Medline](#)
6. Y. Wu, F. Wang, C. Shen, W. Peng, D. Li, C. Zhao, Z. Li, S. Li, Y. Bi, Y. Yang, Y. Gong, H. Xiao, Z. Fan, S. Tan, G. Wu, W. Tan, X. Lu, C. Fan, Q. Wang, Y. Liu, C. Zhang, J. Qi, G. F. Gao, F. Gao, L. Liu, A noncompeting pair of human neutralizing antibodies block COVID-19 virus binding to its receptor ACE2. *Science* **368**, 1274–1278 (2020). [doi:10.1126/science.abc2241](https://doi.org/10.1126/science.abc2241) [Medline](#)
7. K. L. Winarski, J. Tang, L. Klenow, J. Lee, E. M. Coyle, J. Manischewitz, H. L. Turner, K. Takeda, A. B. Ward, H. Golding, S. Khurana, Antibody-dependent enhancement of influenza disease promoted by increase in hemagglutinin stem flexibility and virus fusion kinetics. *Proc. Natl. Acad. Sci. U.S.A.* **116**, 15194–15199 (2019). [doi:10.1073/pnas.1821317116](https://doi.org/10.1073/pnas.1821317116) [Medline](#)
8. A. Taylor, S.-S. Foo, R. Bruzzone, L. V. Dinh, N. J. C. King, S. Mahalingam, Fc receptors in antibody-dependent enhancement of viral infections. *Immunol. Rev.* **268**, 340–364 (2015). [doi:10.1111/imr.12367](https://doi.org/10.1111/imr.12367) [Medline](#)
9. B. S. Graham, Rapid COVID-19 vaccine development. *Science* **368**, 945–946 (2020). [doi:10.1126/science.abb8923](https://doi.org/10.1126/science.abb8923) [Medline](#)

10. A. C. Walls, Y.-J. Park, M. A. Tortorici, A. Wall, A. T. McGuire, D. Veesler, Structure, function and antigenicity of the SARS-CoV-2 spike glycoprotein. *bioRxiv* 956581 [Preprint] 20 February 2020. <https://doi.org/10.1101/2020.02.19.956581>.
11. A. Chevalier, D. A. Silva, G. J. Rocklin, D. R. Hicks, R. Vergara, P. Murapa, S. M. Bernard, L. Zhang, K. H. Lam, G. Yao, C. D. Bahl, S. I. Miyashita, I. Goreschnik, J. T. Fuller, M. T. Koday, C. M. Jenkins, T. Colvin, L. Carter, A. Bohn, C. M. Bryan, D. A. Fernández-Velasco, L. Stewart, M. Dong, X. Huang, R. Jin, I. A. Wilson, D. H. Fuller, D. Baker, Massively parallel de novo protein design for targeted therapeutics. *Nature* **550**, 74–79 (2017). [doi:10.1038/nature23912](https://doi.org/10.1038/nature23912) [Medline](#)
12. J. Dou, A. A. Vorobieva, W. Sheffler, L. A. Doyle, H. Park, M. J. Bick, B. Mao, G. W. Foight, M. Y. Lee, L. A. Gagnon, L. Carter, B. Sankaran, S. Ovchinnikov, E. Marcos, P. S. Huang, J. C. Vaughan, B. L. Stoddard, D. Baker, De novo design of a fluorescence-activating β -barrel. *Nature* **561**, 485–491 (2018). [doi:10.1038/s41586-018-0509-0](https://doi.org/10.1038/s41586-018-0509-0) [Medline](#)
13. W. B. Alsoussi, J. S. Turner, J. B. Case, H. Zhao, A. J. Schmitz, J. Q. Zhou, R. E. Chen, T. Lei, A. A. Rizk, K. M. McIntire, E. S. Winkler, J. M. Fox, N. M. Kafai, L. B. Thackray, A. O. Hassan, F. Amanat, F. Krammer, C. T. Watson, S. H. Kleinstein, D. H. Fremont, M. S. Diamond, A. H. Ellebedy, A Potently Neutralizing Antibody Protects Mice against SARS-CoV-2 Infection. *J. Immunol.* **205**, 915–922 (2020). [doi:10.4049/jimmunol.2000583](https://doi.org/10.4049/jimmunol.2000583) [Medline](#)
14. D. A. Silva, S. Yu, U. Y. Ulge, J. B. Spangler, K. M. Jude, C. Labão-Almeida, L. R. Ali, A. Quijano-Rubio, M. Ruterbusch, I. Leung, T. Biary, S. J. Crowley, E. Marcos, C. D. Walkey, B. D. Weitzner, F. Pardo-Avila, J. Castellanos, L. Carter, L. Stewart, S. R. Riddell, M. Pepper, G. J. L. Bernardes, M. Dougan, K. C. Garcia, D. Baker, De novo design of potent and selective mimics of IL-2 and IL-15. *Nature* **565**, 186–191 (2019). [doi:10.1038/s41586-018-0830-7](https://doi.org/10.1038/s41586-018-0830-7) [Medline](#)
15. J. Shang, G. Ye, K. Shi, Y. Wan, C. Luo, H. Aihara, Q. Geng, A. Auerbach, F. Li, Structural basis of receptor recognition by SARS-CoV-2. *Nature* **581**, 221–224 (2020). [doi:10.1038/s41586-020-2179-y](https://doi.org/10.1038/s41586-020-2179-y) [Medline](#)
16. Q. Wang, Y. Zhang, L. Wu, S. Niu, C. Song, Z. Zhang, G. Lu, C. Qiao, Y. Hu, K. Y. Yuen, Q. Wang, H. Zhou, J. Yan, J. Qi, Structural and Functional Basis of SARS-CoV-2 Entry by Using Human ACE2. *Cell* **181**, 894–904.e9 (2020). [doi:10.1016/j.cell.2020.03.045](https://doi.org/10.1016/j.cell.2020.03.045) [Medline](#)
17. R. Yan, Y. Zhang, Y. Li, L. Xia, Y. Guo, Q. Zhou, Structural basis for the recognition of SARS-CoV-2 by full-length human ACE2. *Science* **367**, 1444–1448 (2020). [doi:10.1126/science.abb2762](https://doi.org/10.1126/science.abb2762) [Medline](#)
18. P. S. Huang, Y.-E. A. Ban, F. Richter, I. Andre, R. Vernon, W. R. Schief, D. Baker, RosettaRemodel: A generalized framework for flexible backbone protein design. *PLOS ONE* **6**, e24109 (2011). [doi:10.1371/journal.pone.0024109](https://doi.org/10.1371/journal.pone.0024109) [Medline](#)
19. N. Koga, R. Tatsumi-Koga, G. Liu, R. Xiao, T. B. Acton, G. T. Montelione, D. Baker, Principles for designing ideal protein structures. *Nature* **491**, 222–227 (2012). [doi:10.1038/nature11600](https://doi.org/10.1038/nature11600) [Medline](#)

20. D. M. Hoover, J. Lubkowski, DNAWorks: An automated method for designing oligonucleotides for PCR-based gene synthesis. *Nucleic Acids Res.* **30**, e43 (2002). [doi:10.1093/nar/30.10.e43](https://doi.org/10.1093/nar/30.10.e43) [Medline](#)
21. C. L. Hsieh, J. A. Goldsmith, J. M. Schaub, A. M. DiVenere, H. C. Kuo, K. Javanmardi, K. C. Le, D. Wrapp, A. G. Lee, Y. Liu, C. W. Chou, P. O. Byrne, C. K. Hjorth, N. V. Johnson, J. Ludes-Meyers, A. W. Nguyen, J. Park, N. Wang, D. Amengor, J. A. Maynard, I. J. Finkelstein, J. S. McLellan, Structure-based Design of Prefusion-stabilized SARS-CoV-2 Spikes. *bioRxiv* 2020.05.30.125484 (2020). <https://doi.org/10.1101/2020.05.30.125484> [Medline](#)
22. C. Suloway, J. Pulokas, D. Fellmann, A. Cheng, F. Guerra, J. Quispe, S. Stagg, C. S. Potter, B. Carragher, Automated molecular microscopy: The new Leginon system. *J. Struct. Biol.* **151**, 41–60 (2005). [doi:10.1016/j.jsb.2005.03.010](https://doi.org/10.1016/j.jsb.2005.03.010) [Medline](#)
23. D. Tegunov, P. Cramer, Real-time cryo-electron microscopy data preprocessing with Warp. *Nat. Methods* **16**, 1146–1152 (2019). [doi:10.1038/s41592-019-0580-y](https://doi.org/10.1038/s41592-019-0580-y) [Medline](#)
24. A. Punjani, J. L. Rubinstein, D. J. Fleet, M. A. Brubaker, cryoSPARC: Algorithms for rapid unsupervised cryo-EM structure determination. *Nat. Methods* **14**, 290–296 (2017). [doi:10.1038/nmeth.4169](https://doi.org/10.1038/nmeth.4169) [Medline](#)
25. D. Kimanius, B. O. Forsberg, S. H. Scheres, E. Lindahl, Accelerated cryo-EM structure determination with parallelisation using GPUs in RELION-2. *eLife* **5**, e18722 (2016). [doi:10.7554/eLife.18722](https://doi.org/10.7554/eLife.18722) [Medline](#)
26. J. Zivanov, T. Nakane, B. O. Forsberg, D. Kimanius, W. J. H. Hagen, E. Lindahl, S. H. W. Scheres, New tools for automated high-resolution cryo-EM structure determination in RELION-3. *eLife* **7**, e42166 (2018). [doi:10.7554/eLife.42166](https://doi.org/10.7554/eLife.42166) [Medline](#)
27. A. Punjani, H. Zhang, D. J. Fleet, Non-uniform refinement: Adaptive regularization improves single particle cryo-EM reconstruction. *bioRxiv* 877092 [Preprint] 16 December 2019. <https://doi.org/10.1101/2019.12.15.877092>.
28. J. Zivanov, T. Nakane, S. H. W. Scheres, A Bayesian approach to beam-induced motion correction in cryo-EM single-particle analysis. *IUCrJ* **6**, 5–17 (2019). [doi:10.1107/S205225251801463X](https://doi.org/10.1107/S205225251801463X) [Medline](#)
29. S. Chen, G. McMullan, A. R. Faruqi, G. N. Murshudov, J. M. Short, S. H. W. Scheres, R. Henderson, High-resolution noise substitution to measure overfitting and validate resolution in 3D structure determination by single particle electron cryomicroscopy. *Ultramicroscopy* **135**, 24–35 (2013). [doi:10.1016/j.ultramic.2013.06.004](https://doi.org/10.1016/j.ultramic.2013.06.004) [Medline](#)
30. E. F. Pettersen, T. D. Goddard, C. C. Huang, G. S. Couch, D. M. Greenblatt, E. C. Meng, T. E. Ferrin, UCSF Chimera—A visualization system for exploratory research and analysis. *J. Comput. Chem.* **25**, 1605–1612 (2004). [doi:10.1002/jcc.20084](https://doi.org/10.1002/jcc.20084) [Medline](#)
31. A. Casañal, B. Lohkamp, P. Emsley, Current developments in Coot for macromolecular model building of Electron Cryo-microscopy and Crystallographic Data. *Protein Sci.* **29**, 1069–1078 (2020). [doi:10.1002/pro.3791](https://doi.org/10.1002/pro.3791) [Medline](#)

32. B. Frenz, S. Rämisch, A. J. Borst, A. C. Walls, J. Adolf-Bryfogle, W. R. Schief, D. Veessler, F. DiMaio, Automatically fixing errors in glycoprotein structures with Rosetta. *Structure* **27**, 134–139.e3 (2019). [doi:10.1016/j.str.2018.09.006](https://doi.org/10.1016/j.str.2018.09.006) [Medline](#)
33. F. DiMaio, Y. Song, X. Li, M. J. Brunner, C. Xu, V. Conticello, E. Egelman, T. Marlovits, Y. Cheng, D. Baker, Atomic-accuracy models from 4.5-Å cryo-electron microscopy data with density-guided iterative local refinement. *Nat. Methods* **12**, 361–365 (2015). [doi:10.1038/nmeth.3286](https://doi.org/10.1038/nmeth.3286) [Medline](#)
34. R. Y. Wang, Y. Song, B. A. Barad, Y. Cheng, J. S. Fraser, F. DiMaio, Automated structure refinement of macromolecular assemblies from cryo-EM maps using Rosetta. *eLife* **5**, e17219 (2016). [doi:10.7554/eLife.17219](https://doi.org/10.7554/eLife.17219) [Medline](#)
35. C. J. Williams, J. J. Headd, N. W. Moriarty, M. G. Prisant, L. L. Videau, L. N. Deis, V. Verma, D. A. Keedy, B. J. Hintze, V. B. Chen, S. Jain, S. M. Lewis, W. B. Arendall 3rd, J. Snoeyink, P. D. Adams, S. C. Lovell, J. S. Richardson, D. C. Richardson, MolProbity: More and better reference data for improved all-atom structure validation. *Protein Sci.* **27**, 293–315 (2018). [doi:10.1002/pro.3330](https://doi.org/10.1002/pro.3330) [Medline](#)
36. D. Liebschner, P. V. Afonine, M. L. Baker, G. Bunkóczi, V. B. Chen, T. I. Croll, B. Hintze, L.-W. Hung, S. Jain, A. J. McCoy, N. W. Moriarty, R. D. Oeffner, B. K. Poon, M. G. Prisant, R. J. Read, J. S. Richardson, D. C. Richardson, M. D. Sammito, O. V. Sobolev, D. H. Stockwell, T. C. Terwilliger, A. G. Urzhumtsev, L. L. Videau, C. J. Williams, P. D. Adams, Macromolecular structure determination using X-rays, neutrons and electrons: Recent developments in Phenix. *Acta Crystallogr. D Struct. Biol.* **75**, 861–877 (2019). [doi:10.1107/S2059798319011471](https://doi.org/10.1107/S2059798319011471) [Medline](#)
37. J. Agirre, J. Iglesias-Fernández, C. Rovira, G. J. Davies, K. S. Wilson, K. D. Cowtan, Privateer: Software for the conformational validation of carbohydrate structures. *Nat. Struct. Mol. Biol.* **22**, 833–834 (2015). [doi:10.1038/nsmb.3115](https://doi.org/10.1038/nsmb.3115) [Medline](#)
38. B. A. Barad, N. Echols, R. Y.-R. Wang, Y. Cheng, F. DiMaio, P. D. Adams, J. S. Fraser, EMRinger: Side chain-directed model and map validation for 3D cryo-electron microscopy. *Nat. Methods* **12**, 943–946 (2015). [doi:10.1038/nmeth.3541](https://doi.org/10.1038/nmeth.3541) [Medline](#)
39. T. D. Goddard, C. C. Huang, E. C. Meng, E. F. Pettersen, G. S. Couch, J. H. Morris, T. E. Ferrin, UCSF ChimeraX: Meeting modern challenges in visualization and analysis. *Protein Sci.* **27**, 14–25 (2018). [doi:10.1002/pro.3235](https://doi.org/10.1002/pro.3235) [Medline](#)